RSC Advances

PAPER

View Article Online
View Journal | View Issue

Check for updates

Cite this: *RSC Adv.*, 2025, **15**, 28413

# Interface engineering of a MXenes/PVDF mixed-matrix membrane for superior water purification: efficient removal of oil, protein and tetracycline

Heba A. El-Nemr,[ab] Mohamed E. El-Khouly,*[a] Mathias Ulbricht [c] and Ahmed S. G. Khalil *[de]

This study developed a high-performance polyvinylidene difluoride (PVDF) mixed matrix membrane incorporating MXene nanosheets for efficient wastewater treatment. The addition of MXene significantly enhanced the water permeability and antifouling properties of PVDF ultrafiltration membranes, as confirmed by scanning electron microscopy (SEM) and transmission electron microscopy (TEM) characterization of the nanoadditive and SEM analysis of the modified membranes. The optimal membrane, blended with 0.2 wt% MXene, exhibited a maximum water permeance of 1242 kg $m^{-2}$ h per bar and maintained a 99% crude oil rejection rate over three separation cycles, demonstrating excellent antifouling performance. This superior separation efficiency across different feeds resulted from favorable interactions between MXene and pollutants, enhancing bovine serum albumin and tetracycline adsorption while synergistically improving water permeability and pollutant capture. Consequently, MXene/PVDF mixed matrix membranes show strong potential as an effective, durable, and stable solution for removing emerging wastewater pollutants, offering enhanced performance in pollutant rejection/removal and fouling resistance, thus addressing critical water purification and environmental sustainability challenges.

Received 23rd May 2025
Accepted 5th August 2025

DOI: 10.1039/d5ra03649f

rsc.li/rsc-advances

Open Access Article. Published on 11 August 2025. Downloaded on 8/28/2025 4:21:29 AM.
This article is licensed under a Creative Commons Attribution-NonCommercial 3.0 Unported Licence.

## 1. Introduction

The shortage of fresh water, with the increasing contamination of water resources, has intensified the demand for advanced and sustainable wastewater treatment technologies.[1,2] As the global population grows and industrial activities expand, the need for innovative solutions to preserve and treat water efficiently has become critical.[3] Sustainable approaches are vital to ensuring the availability of clean water for future generations while minimizing environmental impacts. Traditional treatment methods often fail to remove a broad spectrum of pollutants, including oils, pharmaceutical compounds, and various types of macromolecular organic matter, which pose significant environmental and health risks.[4] These contaminants, often challenging to remove through conventional treatment methods, can have long-term impacts on ecosystems and human health. As a result, there is a growing need for more effective and sustainable treatment technologies to address these complex pollutants.[5,6]

Various technologies have been developed to treat wastewater; each designed to target specific types of contaminants and improve water quality. From traditional methods such as filtration, sedimentation and biological treatments to advanced techniques like membrane filtration and chemical processes, these systems play a crucial role in addressing the growing challenge of water pollution.[7,8] As the demand for cleaner water increases, the continued advancement and integration of these technologies are essential for ensuring sustainable water management and environmental protection. Membrane filtration systems have emerged as a highly effective solution for wastewater treatment, offering the ability to remove a wide range of pollutants.[9,10] As water scarcity and pollution continue to rise, membrane filtration stands out as a promising technology for both industrial and municipal wastewater treatment applications.

These systems, which include processes such as microfiltration, ultrafiltration, nanofiltration, and reverse osmosis, have gained popularity due to their efficiency, scalability, and ability to produce high-quality treated water.[11,12] Microfiltration and ultrafiltration operate at lower pressures compared to the other filtration processes, resulting in lower energy consumption, and typically have a long operational life and require

[a]*Institute of Basic and Applied Sciences, Egypt-Japan University of Science and Technology (E-JUST), New Borg El-Arab City, 21934 Alexandria, Egypt*
[b]*Chemistry Department, Faculty of Science, Sohag University, 82524 Sohag, Egypt*
[c]*Lehrstuhl für Technische Chemie II and Center for Water and Environmental Research (ZWU), Universität Duisburg-Essen, Universitätsstr 7, 45141 Essen, Germany*
[d]*Environmental and Smart Technology Group, Faculty of Science, Fayoum University, 63514 Fayoum, Egypt*
[e]*EvoSmarTec GmbH, Alfredstr. 81, 45130 Essen, Germany. E-mail: mohamed.elkhouly@ejust.edu.eg; asg05@fayoum.edu.eg*

© 2025 The Author(s). Published by the Royal Society of Chemistry

Open Access Article. Published on 11 August 2025. Downloaded on 8/28/2025 4:21:29 AM. This article is licensed under a Creative Commons Attribution-NonCommercial 3.0 Unported Licence.

minimal chemical cleaning.[13] Nevertheless, the capital investment for ultrafiltration systems can be significant compared to traditional treatment options. In contrast, nanofiltration and reverse osmosis are effective, but they require higher pressures than microfiltration and ultrafiltration, leading to higher energy consumption and cost for operation.[14,15] Recent advances in ultrafiltration membranes using novel materials and surface designs have also shown significant potential,[16,17] highlighting the broader importance of the membrane structure–property relationship. Among the commonly used membrane materials, polyvinylidene difluoride (PVDF) stands out due to its excellent chemical resistance, mechanical strength, and thermal stability.[18,19] However, pristine PVDF membranes face limitations; the hydrophobicity makes it prone to organic fouling, low permeability, and suboptimal rejection of specific pollutants, especially when dealing with complex wastewater streams.[20,21]

To overcome these challenges, grafting hydrophilic polymers, blending nanomaterials into the polymer matrix, or introducing specific anti-fouling agents can significantly enhance membrane performance.[22–25] The incorporation of nanomaterials into PVDF membranes to form mixed matrix membranes (MMMs) has gained significant attention.[26–30] By embedding functional nanomaterials into the membrane matrix, the properties of established polymers such as PVDF, including mechanical stability, hydrophilicity, and fouling resistance, can be significantly enhanced.[31] MXenes are a novel class of two-dimensional (2D) materials composed of transition metal carbides and nitrides with the general formula $M_{n+1}X_nT_x$ ($n = 1$, 2 or 3) where M refers to transition metals, X is nitrogen or carbon, and T stands for the termination group (OH, O, or F).[32,33] MXenes exhibit remarkable hydrophilicity, high surface area, electrical conductivity, and tunable surface chemistry, making them ideal potential nanofillers for membrane applications.[34,35] The integration of MXene nanosheets into membrane matrix enhance water permeability, pollutant removal efficiency, and resistance to fouling, addressing the key challenges faced by conventional membranes.[36,37]

$Ti_3C_2T_x$ is one of the most widely investigated MXene materials that has garnered significant attention due to its remarkable surface chemistry for a wide range of applications, including gas separation, ion sieving, desalination, and heavy metal adsorption.[38] Their unique structure and properties enable efficient interactions with various molecules and ions, enhancing separation and filtration processes. Their excellent hydrophilicity enhances water permeation and provides strong resistance to oil fouling, making these membranes highly effective for separating oil from water in wastewater treatment and environmental remediation applications.[39,40] Blending nanomaterials with membrane materials to improve the performance still has some issues, such as detachment caused by poor stability of the nanoadditive into the membrane matrix, uneven distribution of the additive, or neglecting proper phase identification; all this calls the need to optimize fabrication parameters in order to mitigate these limitations.[41,42] Dao *et al.* used alkalized MXene as a model adsorbent to study the adsorption behavior of this modified MXene toward different ions and to investigate their synergetic effect against organic pollutant such as tetracycline and inorganic ions as well.[43] Zhang *et al.* deposited $Ti_3C_2T_x$ MXene 2D nanosheets onto commercial porous PVDF membranes by vacuum filtration to separate a series of stable emulsions, even emulsified crude oil-in-water mixtures; the membranes display excellent separation efficiency (over 99.4% oil rejection) and a high permeance of 887 $Lm^{-2}$ h per bar.[44] Chen *et al.* constructed a PVDF mixed-matrix membrane incorporating MXene nanosheets as nanofillers and 1-hexyl-3-methylimidazolium bis (trifluoromethyl sulfonyl) imide ionic liquid (IL) *via* impregnating intercalation, followed by blending with polymer. Due to hydrophilic groups of MXene's structure, and amino groups of IL, the polarity and hydrophilicity of PVDF MMM are improved and antifouling properties towards bovine serum albumin (BSA) were obtained with barely enhancing the pure water flux of 160 L $m^{-2}$ $h^{-1}$ at 1 bar.[45] Imsong *et al.* designed a PVDF nanofibrous membrane tailored with a 2D nanostructured composite of MXene nanosheets and $TiO_2$, for the treatment of oily wastewater.[46] Despite the growing interest in MXene–PVDF membranes, most prior studies have focused either on dyes or proteins as model pollutants and often required surface functionalization or multistep fabrication. Few works have investigated the use of pristine $Ti_3C_2T_x$ MXene, integrated into PVDF *via* a facile, scalable phase inversion method, for the direct removal of complex pollutants such as oil-in-water emulsions and pharmaceutical residues.

This study focuses on the use of pristine $Ti_3C_2T_x$ MXene nanosheets to develop high-performance MXene@PVDF mixed matrix membranes for wastewater treatment *via* a simplified and scalable fabrication approach. The membranes are designed to target a wide range of pollutants, including oil-in-water emulsion, organic matter (with BSA as model), and tetracycline (as model for organic micropollutants, *e.g.*, pharmaceuticals), with the aim of improving both separation efficiency and operational stability. By investigating the interactions between incorporated MXene nanosheets and various pollutants, an aspect not yet fully addressed in previous work, the work provides an innovative solution for the removal of contaminants from wastewater. The outcomes of this study have the potential to contribute significantly to the advancement of sustainable water treatment technologies, offering a promising approach to addressing the growing challenges of water pollution.

## 2. Methodology

### 2.1. Materials

*N*-methyl-2-pyrrolidone (NMP) and polyvinylpyrrolidone (PVP), were supplied by Loba Chemie PVT Limited, India. Polyvinylidiene diflouride (PVDF MKCR5996, Mw ~534 000 Da) was provided by Sigma Aldrich (USA). Hydrochloric acid (HCl), bovine serum albumin (BSA), and tetracycline (TC) were obtained from BioChemika (Steinheim, Germany). MAX powder ($Ti_3AlC_2$) and lithium flouride (LiF) were purchased from Kandel (Germany). Real oil samples of industrial crude oil were collected from a local Egyptian-based petroleum company and used to prepare oil-in-water emulsions. A summary of the basic


© 2025 The Author(s). Published by the Royal Society of Chemistry

Open Access Article. Published on 11 August 2025. Downloaded on 8/28/2025 4:21:29 AM. This article is licensed under a Creative Commons Attribution-NonCommercial 3.0 Unported Licence.

physicochemical properties of this real industrial crude oil was given in a Table S1 (see SI). Crude oil emulsions with different concentrations of 0.1 g $L^{-1}$ and 1 g $L^{-1}$ were prepared *via* sonication in an ice water bath for 2 h for each concentration before use on each membrane sample.

### 2.2. Synthesis of MXene nanosheets and PVDF mixed matrix membranes

Firstly, LiF (1.6 g) was dissolved in 20 mL 6 M HCl. Then, 1 g $Ti_3AlC_2$ was gradually added to 20 mL of this solution under magnetic stirring and continuously reacted at 35 °C for 24 h. The resulting suspension was centrifuged and washed with deionized water several times until the pH of the filtrate is 6. Subsequently, a 2 h sonication was employed, followed by centrifugation for 5 minutes. Finally, the sample was freeze dried for 24 h to obtain $Ti_3C_2T_x$ MXene.[47,48]

Membranes were fabricated using the non-solvent induced phase separation (NIPS) technique. For the preparation of different dope solutions for casting MMM, MXene powders were exfoliated in NMP solvent by sonication for 2 h in an ice-cooled water bath to obtain 2D nanosheets. Next, the mixture was magnetically stirred for 48 h at 50 °C in the presence of PVDF and PVP to ensure homogeneous blending until a single-colored solution was obtained. Then, the resulting solution was degassed in a vacuum oven and thereafter casted using a casting machine, Coatmaster from Erichsen (Germany), onto a clean glass plate with 200 μm casting knife. The membranes were immediately immersed in a DI water bath, to complete the phase inversion process and remove any residual solvent, followed by storing in DI water until further characterization. MXene nanosheets were added to the polymer solution at different fractions as summarized in Table 1.

### 2.3. Characterization of MXene nanosheets and MMM

The morphology of MXene nanosheets was visualized by scanning electron microscopy SEM (Apreo S Lo Vac, Thermo Fischer Scientific), equipped with an energy-dispersive X-ray spectrometer (EDX), at an accelerating voltage of 5 kV and transmission electron microscopy (TEM) (instrument JEOL JEM-2010F) with an accelerating voltage of 200 kV. For TEM sample preparation, MXene powder was dispersed in ethanol through sonication for 10 minutes and drop-casted onto a carbon-coated copper grid. The specific surface area of the MXene nanosheets was investigated using nitrogen adsorption and Brunauer–Emmett–Teller (BET) analysis performed on a St 4 instrument (NOVA Touch 4LX) after degassing the sample at 33 °C for 3.5 hours. The pore volume and average pore size were determined using the Barrett–Joyner–Halenda (BJH) method applied to the adsorption/desorption isotherms. The rheological properties of the casting solutions (M0–M3) were analyzed using a rotational rheometer (MCR301). The viscosity of each solution was measured as a function of shear stress at 25 °C using a cone-and-plate geometry at a constant shear rate range of 0 to 400 Pa. Prior to measurement, samples were equilibrated on the rheometer stage to ensure temperature uniformity and eliminate any shear history. All measurements were performed in triplicate to ensure reproducibility. The membranes' surface and cross-sectional morphologies were visualized using the same SEM technique. For cross-sectional imaging, the membranes were fractured in liquid nitrogen.

Table 1 Overview on composition of the PVDF mixed matrix membranes

| Membrane | PVDF (wt%) | NMP (wt%) | MXene (wt%) | PVP (wt%) |
|---|---|---|---|---|
| M0 | 16 | 82 | 0 | 2 |
| M1 | 16 | 81.9 | 0.1 | 2 |
| M2 | 16 | 81.8 | 0.2 | 2 |
| M3 | 16 | 81.7 | 0.3 | 2 |

The hydrophilicity of membrane surface was assessed using sessile drop technique with a contact angle goniometer (OCA 25 Plus, Dataphysics GmbH, Germany). The average pore size and pore size distribution of the membrane samples were determined by a gas flow/liquid displacement method using a POROLUX 1000 porometer. To provide a more comprehensive understanding of the membrane pore structure, additional parameters; including bubble point and smallest pore size were also determined. Water uptake of the membranes was measured *via* gravimetric experiment, samples were taken out from the water, wiped to remove excessive water, weighed ($W_w$), and then dried in an oven and reweighed ($W_d$). The water uptake was obtained from the following equation:[49]

$$\text{Water uptake (\%)} = (W_w - W_d)/W_w \times 100 \quad (1)$$

The mechanical properties of the fabricated membranes were evaluated using a universal testing machine (UTM, Shimadzu, AG-X Plus) following ASTM D882 standards. Rectangular membrane strips (15 cm × 2 cm) were clamped with an initial gauge length of 20 mm and subjected to uniaxial tensile testing at a constant speed of 25 mm $min^{-1}$ at room temperature. Three specimens from each membrane (M0–M3) were tested to ensure reproducibility.

### 2.4. Performance of the PVDF membranes

**2.4.1. Measurement of water permeance.** Dead-end filtration cell (feed volume 250 mL, active membrane area 12.56 $cm^2$) was used to measure pure water permeance. First, all membrane samples were compacted by flowing DI water at 2 bar using argon gas for 1 hour to ensure stable permeability. Then, the pressure was reduced to 0.5 bar, and the permeance was evaluated by monitoring the volume/weight of water passing through the membrane. Pure water permeance was calculated as follows:[28]

$$\text{Pure water permeance (PWP)} = m/A \times t \times P \quad (2)$$

where $m$ is the mass of water permeated through the membrane (kg), $A$ is active membrane area ($m^2$), $t$ is the filtration time (h), $P$ is the applied pressure (bar). All error bars in the figures represent standard deviations based on three measurements from the prepared membrane sheets of each type ($n = 3$).

Open Access Article. Published on 11 August 2025. Downloaded on 8/28/2025 4:21:29 AM. This article is licensed under a Creative Commons Attribution-NonCommercial 3.0 Unported Licence.

**2.4.2. Evaluation of separation efficiency and resistance to fouling.** The PVDF-based membranes were tested for anti-fouling characteristics by filtering different pollutant dispersions or solutions at a pressure of 0.5 bar. First, the separation efficiency was tested using crude oil-in-water emulsions at concentrations of 0.1 g $L^{-1}$, and 1 g $L^{-1}$ (Section 2.1). The concentration of both the feed ($C_o$) and permeate ($C_p$) was measured *via* chemical oxygen demand (COD) analysis (MD 200 COD VARIO analyzer). These measurements were then used to determine the rejection.[50] BSA rejection was studied using two concentrations: 0.5 g $L^{-1}$ and 1 g $L^{-1}$ at pH 8.0, using a buffered solution (50 mM tris–HCl). For each concentration, 25 mL of solution was filtered. Analysis of tetracycline analysis was conducted through two concentrations, 50 mg $L^{-1}$ and 100 mg $L^{-1}$, with a volume of 25 mL filtered through the membrane. The absorbance of the filtered solution was measured using UV-vis spectrophotometer and rejection was calculated as following:

$$\text{Rejection } (\%) = ((C_o - C_p)/C_o) \times 100 \quad (3)$$

Fouling experiments were carried out with crude oil emulsions using the same dead-end filtration cell. This was done by recording first the pure water permeance ($P_0$); afterwards, pure water was replaced with the oil-in-water emulsion and the permeance was measured ($P_1$) over a 30-minute filtration period, and then backwashing was performed outside the cell by gently rinsing the membrane surface with DI water to remove accumulated foulants before recording the pure water permeance again ($P_2$).

Fouling parameters, *i.e.*, flux recovery ratio (FRR), resistance due to reversible fouling ($R_r$) and irreversible fouling ($R_{ir}$), of the MMMs are calculated as follows:[16,50]

$$\text{FRR } (\%) = (P_2/P_0) \times 100 \quad (4)$$

$$R_r\ (\%) = ((P_2 - P_1)/P_0) \times 100 \quad (5)$$

$$R_{ir}\ (\%) = ((P_0 - P_2)/P_0) \times 100 \quad (6)$$

After the evaluation of flux recovery through several filtration and backwashing steps, the MMM underwent another two cycle tests to assess their operational stability in the filtration of pure water and oil emulsion.

# 3. Results and discussion

## 3.1. Surface characterization of PVDF mixed matrix membranes

Fig. 1a shows the SEM image of the synthesized $Ti_3C_2T_x$ MXene, displaying a flake-like morphology indicative of multilayered nanosheets structures. Although the resolution of SEM is limited in resolving fine lamellar details, it suggests stacked sheet arrangements with interlayer spacing commonly seen after exfoliation. This structure is crucial for MXene's performance in applications like water purification.[44,51] The surface appears relatively uniform, but slightly textured, possibly due to surface defects, small particulates, or leftover etching residues from the chemical exfoliation process (lithium fluoride in hydrochloric acid used in this work). The roughness could influence the material's surface area and accessibility of ions or molecules in applications including those as filtration membranes.[52–54] While the SEM image suggests layered features, the TEM image (Fig. 1b) provides high-resolution image of the nanosheets structure and more clearly confirms the characteristic multilayered structure of $Ti_3C_2T_x$ at the nanoscale. The image clearly shows well-aligned parallel layers, a defining feature of MXene nanosheets. This supports the successful exfoliation of the MAX phase and retention of the lamellar nature of MXene following synthesis. These layers likely represent the atomic planes of MXene, which consist of transition metal carbides/nitrides. The periodic stripes in the image are lattice fringes, which indicate the ordered, crystalline nature of the material. These lattice fringes are the result of alternating layers of metal and carbon, as is characteristic of the MXene $Ti_3C_2T_x$ that is used in this work. The interlayer spacing can vary depending on the surface termination groups (–O, –OH, –F) present on the MXene, which influence the intercalation properties, making MXenes tunable for different applications. The clear visibility of lattice fringes confirms the high crystallinity of the material. The layers are well-ordered and uniform, suggesting that the exfoliation process did not significantly damage the crystal structure.[55] While the image does not provide a direct measure of the nanosheet's thickness, the regular layering suggests that this is either a few-layer MXene or a thicker nanosheet. A monolayer MXene would show fewer or no discernible lattice fringes. Hence, the presence of multiple layers is likely in the material obtained and used in this work. The EDX analysis confirms the presence of Ti, C, O, and F (Fig. 1c). However, the observed atomic percentages (C: 71.8%, Ti: 13.7%) deviate from the ideal Ti:C ratio, which may be attributed to the surface-sensitive nature of EDX analysis, causing overrepresentation of light elements like carbon, and the presence of surface terminations or carbon contamination of the sample. The elemental mapping further confirms this by showing a uniform distribution of Ti and C, supporting the formation of $Ti_3C_2T_x$ with possible modifications. The presence of oxygen suggests surface oxidation, which is typical in MXene synthesis. The fluorine content suggests successful etching using fluoride-containing reagents, leading to –F functionalized MXene surfaces.

The porous structure and surface characteristics of $Ti_3C_2T_x$ MXene were thoroughly investigated using nitrogen adsorption–desorption analysis to evaluate its surface area and pore structure. The nitrogen adsorption–desorption isotherm of $Ti_3C_2T_x$ MXene (Fig. S1) exhibits a typical type IV curve with an H3 hysteresis loop at high relative pressures ($P/P_0 > 0.8$), which is characteristic of mesoporous materials.[56] The specific surface area, pore volume, and average pore size of $Ti_3C_2T_x$ MXene were determined to be 17.9 $m^2\ g^{-1}$, 0.0789 $cm^3\ g^{-1}$, 8.8 nm, respectively, confirming the mesoporous nature of the MXene material. Such surface characteristics are indicative of the layered structure and interlayer spacing inherent to MXene materials, which can be tailored through synthesis and post-treatment processes to achieve desired porosity and surface area. Similar


© 2025 The Author(s). Published by the Royal Society of Chemistry

Open Access Article. Published on 11 August 2025. Downloaded on 8/28/2025 4:21:29 AM.
This article is licensed under a Creative Commons Attribution-NonCommercial 3.0 Unported Licence.

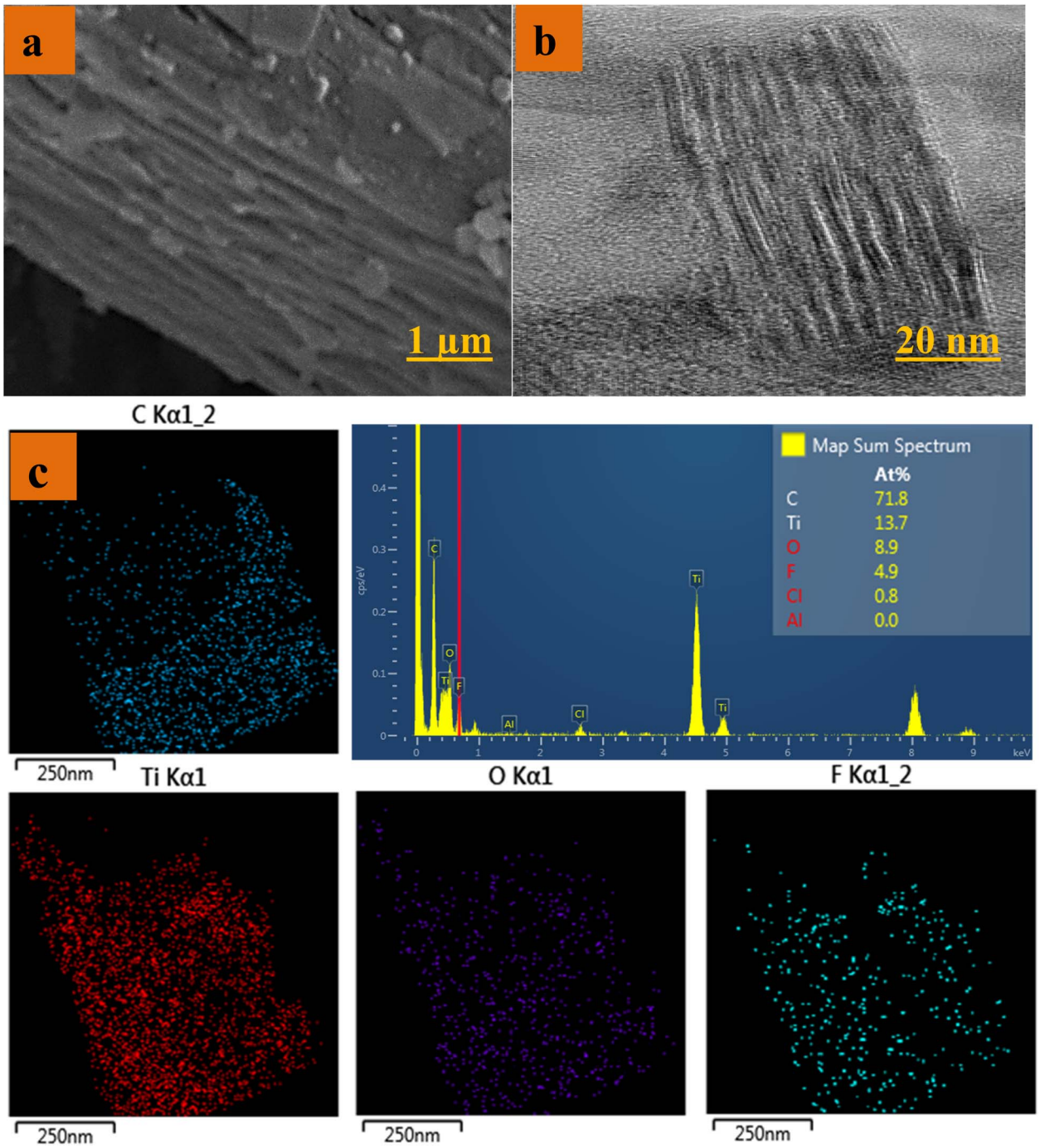


Fig. 1 (a) SEM and (b) TEM images of MXene nanosheets; (c) EDX spectrum and elemental mapping analysis of MXene nanosheets (including atomic percentage of the different elements).

isotherm behaviors have been reported in other $Ti_3C_2T_x$ MXene systems in the literature.[57–59]

The viscosity–shear stress profiles for the casting solutions (M0–M3) are presented in Fig. S2. All samples exhibit shear-thinning behavior, characterized by a decrease in viscosity with increasing shear stress, typical of non-Newtonian fluids. Among them, the M2 solution demonstrated the highest initial viscosity, indicating stronger interchain interactions and increased entanglement possibly due to higher additive loading. The higher viscosity of M2 may enhance membrane structure formation during phase inversion, while the lower viscosity observed in M0 suggests a less structured polymer network. The order of viscosity values at low shear stress was M2 > M1 ≈ M3 > M0, reflecting the influence of MXene nanosheets and concentration on the rheological behavior of the dope solutions.

The surface and cross-sectional morphology of neat and MXene-modified PVDF membranes are displayed in Fig. 2. The

Open Access Article. Published on 11 August 2025. Downloaded on 8/28/2025 4:21:29 AM.
This article is licensed under a Creative Commons Attribution-NonCommercial 3.0 Unported Licence.

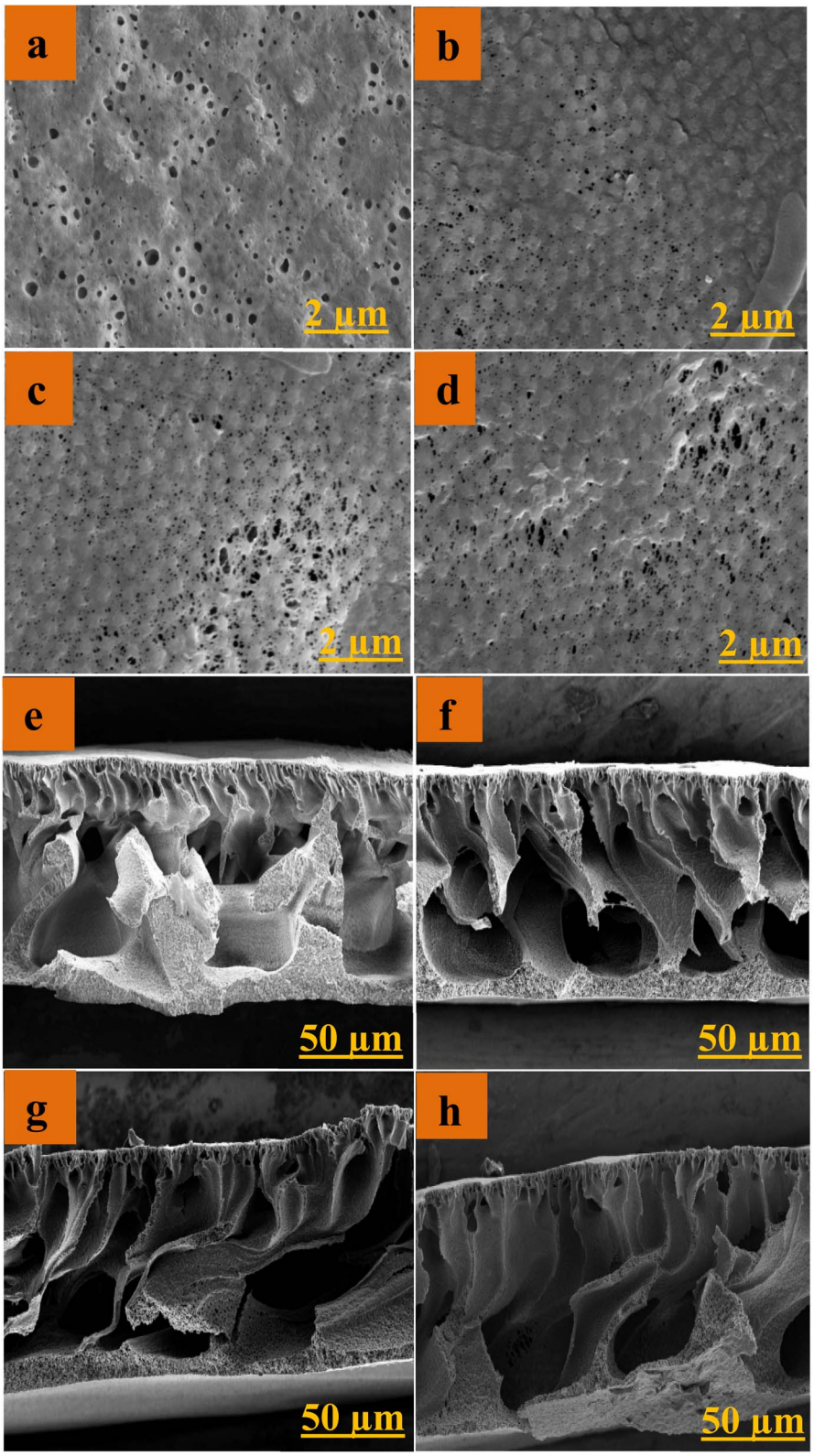


Fig. 2 (a)–(d) SEM images of the top surface of membranes M0, M1, M2 and M3 respectively; (e)–(h) cross-section SEM images for the respective unmodified, and modified PVDF membranes.

outer surface of unmodified membrane appears to have a porous structure with relatively large and irregular pore sizes. These pores are crucial for determining the membrane's permeability and separation performance. Fig. 2b–d show membranes after modification with MXene nanosheets, where the surfaces have become more textured with smaller pores,


© 2025 The Author(s). Published by the Royal Society of Chemistry

Open Access Article. Published on 11 August 2025. Downloaded on 8/28/2025 4:21:29 AM. This article is licensed under a Creative Commons Attribution-NonCommercial 3.0 Unported Licence.

indicating an altered morphology due to the presence of MXene.[60,61] The cross-sectional morphology for membrane samples displayed in Fig. 2e–h illustrates a finger-like structure typical of anisotropic membranes obtained by NIPS method. The cross-section for unmodified membrane typically shows thick, porous support layer with a gradual transition to the dense top layer. Upon modification with MXene nanosheets, the membrane morphology shows a reduction in macrovoid size and a denser packing of polymer chains. The morphology of the PVDF membranes shown in Fig. 2 is strongly influenced by the phase inversion process, particularly the polymer concentration, the presence of additives, and the solvent-nonsolvent exchange rate. In the NIPS method, rapid demixing generally results in a highly porous structure with large macrovoids, while slower demixing leads to a denser top layer and reduced porosity. The incorporation of MXene nanosheets as a nanofiller, modifies the phase separation kinetics by increasing the viscosity of the casting solution and thereby affecting solvent diffusion. As a result, the MMM exhibit a reduction in pore size (Fig. 2a–d), likely due to delayed phase separation and enhanced polymer–nanofiller interactions.

The provided image in Fig. S3(a–e) shows cross-sectional EDX elemental mapping for four membranes. Each spectrum displays peaks corresponding to specific elements detected in the membrane materials. M0 serves as the reference, showing elemental composition without any added modifiers. Peaks for carbon (C) and fluorine (F) as constituents of the base material dominate. The relatively high levels of nitrogen (N) and oxygen (O), which are not components of pristine PVDF is attributed to the incorporation of 2 wt% PVP as a pore-forming additive in all formulations. PVP contains nitrogen and oxygen in its molecular structure, contributing to the observed elemental signals. M1 shows new peaks, indicating incorporation of modifier. Peaks corresponding to titanium (Ti) are derived from MXene nanosheets, and changes in peak intensities and compositions highlight differences in modification across M1, M2, and M3. Further enhancements with M2 and M3, with potentially new or intensified peaks, indicating increased concentrations of nanosheets. In addition, the EDS mapping in Fig. S4(a–e) showed the distribution of the different elements in the surface of the membranes. At low concentrations, MXenes or nanofillers may not reach the membrane's surface during fabrication. Instead, they are likely distributed within the bulk matrix, explaining their detection in the cross-section but not on the surface. This is due to the method of incorporating MXene by blending with the polymer, which significantly impacts its distribution. As the concentration increases, a higher quantity of MXenes ensures more uniform distribution, with some particles migrating to the surface; therefore, increased concentration enhances the signal strength, making it detectable on the surface. The presence of MXene on both surface and cross-section is precondition for the expected enhanced performance, potentially improving properties such as adsorber or antifouling properties. However, too high concentrations might result in agglomeration, which can cause MXene nanosheets to localize on the surface more than the cross-section as indicated for M3. Additionally, photographic images of the casted membrane sheets (Fig. S5) visually confirm the uniform dispersion of MXene nanosheets within the PVDF matrix. The modified membranes (M1–M3) exhibited homogenous coloration and smooth, defect-free surfaces, without visible aggregation or uneven texture compared to the pristine membrane (M0). This uniform appearance reflects the effective integration of MXene, attributed to optimized dispersion *via* prolonged sonication and stirring during the dope solution.

Fig. 3a illustrates the average barrier pore size of the membranes. The unmodified membrane (M0) has the largest average pore size at around 255 nm. Membranes M1 and M2 show a noticeable decrease in pore size; the values 223 nm and 226 nm, respectively, indicate that the incorporation of MXene nanosheets likely led to denser membrane barrier layer structure. This reduction in pore size could be due to the nanosheets acting as fillers within the membrane matrix, partially blocking or narrowing some of the larger pores present in the unmodified membrane. This suggests that the MXene nanosheets may be dispersing more evenly at this level of modification, allowing the pores to maintain their structure without excessive blocking. Membrane M3 shows a similar average pore size, with a slight reduction compared to M2. This could indicate that the membrane's pore structure has stabilized at this level of MXene incorporation, where the nanosheets are neither excessively filling nor widening the pores. To further elucidate the changes in membrane structure upon MXene incorporation, additional pore size parameters including the bubble point and smallest pore size are presented in Table S2 (SI). All three metrics; bubble point, mean, and smallest pore size show a consistent trend: the incorporation of MXene slightly reduces the pore size from M0 to M2. This is in agreement with SEM observations. The reduction in pore size for M1 and M2 supports the formation of narrower and more uniform transport pathways. The pore size distribution profiles (Fig. S6) highlight the structural changes induced by MXene addition. Membrane M0 displays a sharp, narrow distribution centered about 265 nm, indicating a relatively uniform porous structure. With increasing MXene loading, particularly at 0.2 wt% (M2), the distribution becomes broader yet more consistent, reflecting enhanced pore interconnectivity. In contrast, M3 shows signs of pore narrowing and reduced frequency, likely due to nanosheets agglomeration and partial blockage. These results confirm that moderate MXene incorporation contributes to a more favorable pore architecture, supporting improved permeability and rejection performance.

Fig. 3b presents the water contact angle and water uptake of the membranes. The contact angle values decrease progressively from M0 to M3. The contact angle of the unmodified membrane M0 is relatively high, *i.e.*, 71°, indicating a moderately hydrophobic surface. In contrast, for membranes M1, M2, and M3, contact angle values decrease with the incorporation of MXene nanosheets, reaching lowest for M2 (63°), suggesting an improvement in hydrophilicity, which is likely due to the hydrophilic nature of MXene nanosheets. This is due to the inherent hydrophilic nature of MXene nanosheets, which introduce surface groups such as hydroxyls (−OH) and oxygen-containing functional groups.[62] However, the contact angle tends to stabilize after further increase of filler loading, with

Open Access Article. Published on 11 August 2025. Downloaded on 8/28/2025 4:21:29 AM.
This article is licensed under a Creative Commons Attribution-NonCommercial 3.0 Unported Licence.

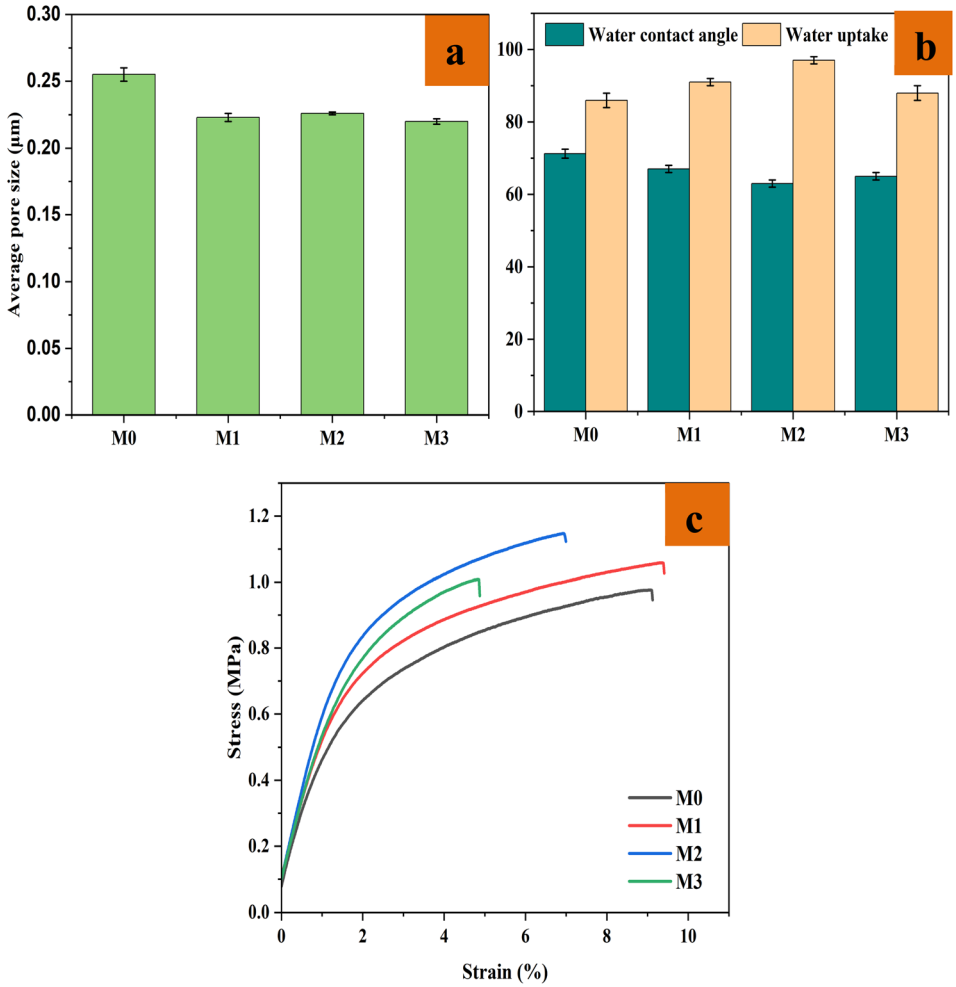


Fig. 3 (a) Average pore size (b) water contact angle, and water uptake, (c) mechanical strength profiles of fabricated membranes.

membrane M3 having similar contact angle (65°). This suggests that beyond a certain level of MXene incorporation, no further reduction in contact angle occurs, possibly due to the aggregation of MXene nanosheets in the membrane.

Water uptake is a crucial parameter that determines the membrane's ability to retain water, correlating with hydrophilicity and structural porosity. As shown in Fig. 3b, all membranes exhibit high water uptake, with M0; 86%, indicative of a highly porous structure dominated by macrovoids, as observed in the cross-sectional SEM images (Fig. 2). Upon incorporation of MXene, membranes M1–M3 show a gradual increase in water uptake, with M2 achieving the highest value at 97%. This trend suggests that MXene nanosheets influence the phase inversion process, potentially promoting additional micro- and meso-porosity that accommodates more water. The SEM images reveal that macrovoids remain prevalent across all samples, including the modified membranes, indicating that the increase in water uptake may not stem from a reduction in macrovoids but from increased water-accessible porosity due to MXene-induced structural variation. M2 represents the most porous structure, while M3 shows a slight decrease in water uptake, potentially due to excessive nanosheets addition that could block pores reducing effective water uptake. This slight decrease in water uptake for M3 may indicate that at high concentrations of MXene, there is a blocking effect, where the excess nanosheets begin to clog the pores, reducing overall water uptake. This highlights the importance of controlling the MXene loading to avoid diminishing returns in water uptake improvement.

In contrast to the pristine PVDF membrane (M0), the membranes containing MXene nanosheets exhibited better mechanical behavior. As shown in Fig. 3c, membrane M2 exhibited the highest tensile strength (~1.2 MPa), indicating improved elasticity and load-bearing capacity. This enhancement can be attributed to the homogeneous dispersion of MXene within the polymer matrix, which facilitates stress transfer and reinforces the membrane structure. The improved plasticity suggests that the membrane can endure prolonged tensile stress without premature failure. However, at higher additive loading (M3), a slight reduction in tensile performance was observed. This may result from excessive nanosheets content disrupting the polymer chain alignment and creating micro-defects or agglomerations that weaken structural integrity. Thus, while moderate addition of MXene improves mechanical behavior, excessive loading may induce brittleness and compromise membrane robustness.


© 2025 The Author(s). Published by the Royal Society of Chemistry

Open Access Article. Published on 11 August 2025. Downloaded on 8/28/2025 4:21:29 AM.
This article is licensed under a Creative Commons Attribution-NonCommercial 3.0 Unported Licence.

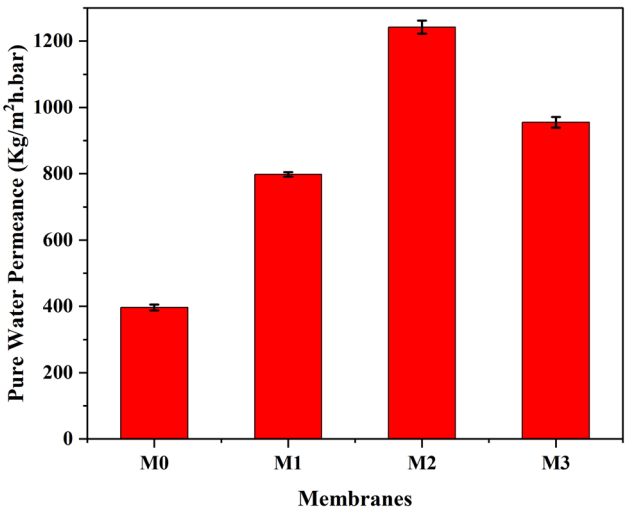


Fig. 4 Pure water permeance for all membrane samples.

### 3.2. Separation performance of PVDF mixed matrix membranes

**3.2.1. Permeance of different PVDF MMM.** Fig. 4 shows the permeability of the different PVDF MMM. The neat PVDF M0 had the lowest pure water permeability about 396 kg $m^{-2}$ h per bar. The incorporation of MXene nanosheets significantly improves the pure water permeability of the PVDF membranes as seen in the increase in water permeance for M1 and M2. Membrane M2, which likely contains an optimal concentration of MXene, exhibits the highest permeability at 1242 kg $m^{-2}$ h per bar. The hydrophilic nature of MXenes is beneficial for water transport through the membrane, the changes of pore structure that improve permeability without enlarging the pore size in the barrier layer (Fig. 3a) are likely a higher porosity and/or a lower thickness of the barrier layer compared to M0. The trend is not strictly linear, as membrane M3 shows a drop in permeability (797 kg $m^{-2}$ h per bar) compared to M2, indicating that there may be an upper limit to the beneficial effects of MXene incorporation. Increasing the MXene loading to 0.3 wt% led to a noticeable decrease in permeability and more compact structure, as seen in SEM images (Fig. 2), indicating agglomeration and partial pore blockage. This suggests that while MXene enhances membrane performance up to a certain concentration, excessive loading may lead to nanosheet aggregation and pore clogging, thereby reducing the overall performance. Based on both morphological features and water permeance data, the membrane containing 0.2 wt% MXene exhibited the optimal concentration, achieving a balance between effective dispersion and minimal agglomeration without compromising structural integrity. Overall, higher water permeance is beneficial in filtration applications, indicating that MXene incorporation would make PVDF membranes more efficient for water treatment or other separation processes.[44]

**3.2.2. Separation of oil-in-water emulsion.** Fig. 5a, and S7a, respectively, show the permeance of various PVDF-based membranes over time, with three repeated cycles of crude oil emulsion separation, with feed concentrations of 0.1 g $L^{-1}$ and 1 g $L^{-1}$, respectively. The results imply that the membranes show better permeance and more efficient filtration when exposed to the lower concentration feed (0.1 g $L^{-1}$), as compared to the higher concentration (1 g $L^{-1}$). Membrane M0 shows the lowest permeance throughout the test for both concentrations, this could be due to limited intrinsic water permeability and fouling during oil separation.[63] After MXene was introduced, the permeance improved noticeably, with membrane M2 showing the highest initial permeance.

Across all membrane types, the rejection percentages are high, close to 100%, with minimal difference between the 0.1 g $L^{-1}$ and 1 g $L^{-1}$ concentrations (see Fig. 5c and S7c), which indicates that all membranes are effective in rejecting oil from the water, regardless of the feed concentration. This suggests that the concentration of the oil-water emulsion does not significantly impact the rejection performance of the membranes. The permeance values drop after each cycle and partially recover in all membranes. This indicates that fouling occurs during the separation process, reducing water flux. However, membranes containing MXene nanosheets show higher permeance recovery than M0, which suggests that the inclusion of MXene enhances fouling resistance, likely due to improved hydrophilicity and anti-fouling properties. The data indicates that MXene improves not only permeance but also membrane stability and anti-fouling properties, making it a promising additive for membranes used in oil-water separation applications.[64–66]

**3.2.3. Fouling resistance characteristics of PVDF mixed matrix membranes.** Flux recovery ratio FRR is a key performance indicator that shows how well a membrane recovers its filtration capacity after cleaning, which relates to its fouling resistance. All membranes start with high FRR values, with better recovery ratios for the membranes containing MXene nanosheets (M1, M2, and M3) than the unmodified membrane (M0) as shown in Fig. 5b and S7b. Membrane M2 has the highest initial FRR (~92%, 84.5%, in 0.1 g $L^{-1}$, and 1 g $L^{-1}$, respectively), confirming that this modification performs best in terms of flux recovery after the first cycle of fouling and cleaning. There is a noticeable decrease in the FRR for all membranes in both oil feed concentrations, indicating that fouling and incomplete cleaning are progressively reducing the membranes' ability to fully recover their flux. Membranes M2 and M3 maintain relatively high FRR values (~75–80%), while M0 has a significantly lower FRR especially after the third cycle, indicating poorer recovery after repeated use, which suggests that it is more prone to irreversible fouling. Over the three cycles, M2 stands out as the best-performing membrane, possibly due to an optimal concentration of MXene that enhances fouling resistance without compromising the membrane's structural integrity or causing excess blocking.

Fig. 5c and S7c show antifouling parameters, such as reversible fouling resistance $R_r$ and irreversible fouling resistance $R_{ir}$. As MXene content increases, M1, M2, and M3 show progressively higher $R_r$ values for both oil feed concentrations, with M2 having the most significant improvement. This suggests that MXene nanosheets enhance the membrane's

Open Access Article. Published on 11 August 2025. Downloaded on 8/28/2025 4:21:29 AM.
This article is licensed under a Creative Commons Attribution-NonCommercial 3.0 Unported Licence.

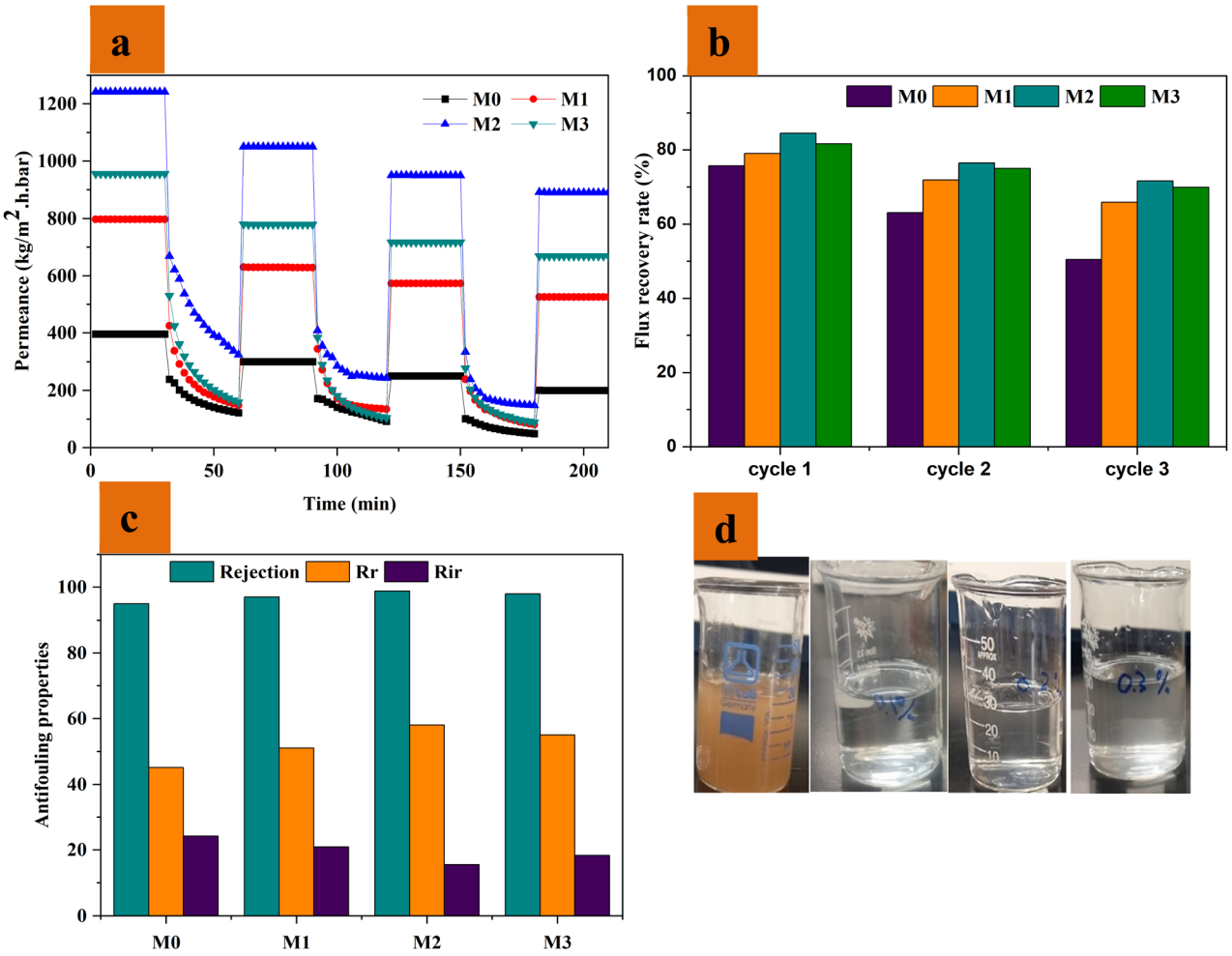


Fig. 5 Permeance with 1 g $L^{-1}$ crude-oil emulsion: (a) cyclic performance, (b) FRR after three cycles, (c) oil rejection, $R_r$, and $R_{ir}$, (d) digital photograph of feed and permeate obtained with the membranes.

ability to resist fouling that can be removed or mitigated through simple rinsing with DI water. Membrane M2 appears to strike an optimal balance, indicating that it has the highest reversible fouling resistance, meaning that fouling in this membrane is more easily addressed, likely due to enhanced hydrophilicity and reduced oil adhesion. The neat PVDF membrane; M0 has the highest irreversible fouling ($R_{ir}$) in both emulsion concentrations, meaning that once fouling occurs, it cannot easily be removed or reversed. This is common in hydrophobic membranes like pure PVDF. The inclusion of MXene in M1, M2, and M3 substantially reduces irreversible fouling in both 0.1 g $L^{-1}$ and 1 g $L^{-1}$ emulsion concentrations, with M2 showing the lowest value 7.4, 15.5, respectively. This indicates that MXene improves the antifouling characteristics of the membrane, possibly due to the increased hydrophilicity that reduces oil deposition and adherence. The performance of M3 is slightly less efficient compared to M2, indicating that an intermediate MXene content (as in M2) might offer the best antifouling properties for the PVDF membranes. The optimal MXene concentration, as suggested by the performance of M2, leads to a significant reduction in membrane fouling while maintaining high rejection efficiency. This agrees with that MXene enhances both the membrane's oil-water separation performance and its long-term operational stability.[40,44] The images in Fig. 5d and S7d represent successful separation of oil from the water phase using both unmodified and modified membranes, highlighting the improved separation ability when MXene nanosheets are involved for membrane modification.

**3.2.4. Assessment of BSA solution filtration.** Fig. 6a illustrates the permeance of BSA solutions at concentrations of 0.5 g $L^{-1}$ and 1 g $L^{-1}$ through different PVDF-based membranes. Modification of PVDF significantly improves the permeate flux at both low and high BSA concentrations. The permeance of BSA solutions generally decreases as the concentration of BSA increases, reflecting membrane fouling. However, the modified membranes (M1, M2, M3) exhibit better performance compared to the neat membrane (M0). Membrane M2 clearly outperforms the others in both water and BSA permeance, about 500 kg $m^{-2}$ h per bar, and 400 kg $m^{-2}$ h per bar, for.0.5 g $L^{-1}$, 1 g $L^{-1}$, respectively, demonstrating its effectiveness in resisting fouling and maintaining high permeability. This highlights the importance of membrane modification in improving both water


© 2025 The Author(s). Published by the Royal Society of Chemistry

Open Access Article. Published on 11 August 2025. Downloaded on 8/28/2025 4:21:29 AM. This article is licensed under a Creative Commons Attribution-NonCommercial 3.0 Unported Licence.

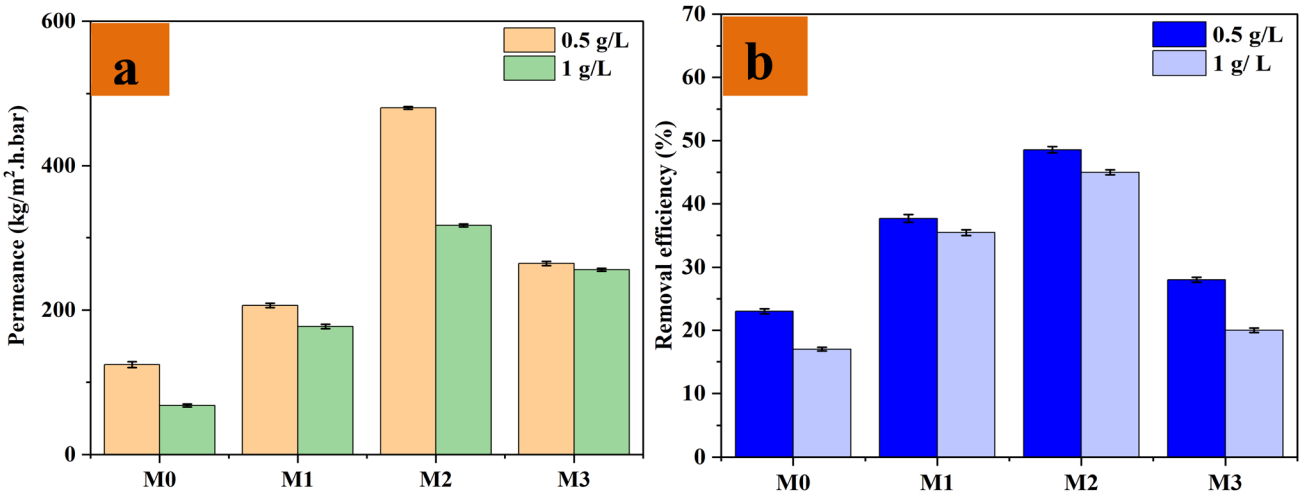


Fig. 6 (a) Permeance during BSA solution filtration, (b) overall BSA removal efficiency of the unmodified and modified membrane samples towards 0.5 g $L^{-1}$ and 1 g $L^{-1}$ BSA.

permeability and fouling resistance during BSA filtration. Membrane M3 performs better than M1 in terms of water permeance, its BSA permeance is lower, indicating higher fouling than M2 but still better than M0. Membrane M2 emerges as the best candidate for applications requiring high permeability and fouling resistance.

Fig. 6b shows the removal efficiency (%) of BSA at two different concentrations (0.5 g $L^{-1}$ and 1 g $L^{-1}$) using four different PVDF membranes. It is clear that neat PVDF membrane (M0) is less effective in removing BSA, especially at higher concentration. The separation efficiency improves with involving MXene nanosheets compared to M0; however, the efficacy decreases as the concentration of BSA increases. This is because a higher concentration leads to faster membrane fouling due to the increased number of protein molecules interacting with the membrane surface. The MXene-modified membranes can better resist fouling, which is critical for handling proteins like BSA that tend to form layers on membrane surfaces.[66] The incorporation of MXene nanosheets significantly improves the performance of PVDF membranes in BSA separation.[45] For 0.5 g $L^{-1}$ BSA, the removal efficiency reaches 45%, 60% with 0.1%, 0.2% of MXene nanosheets, respectively compared to 23% in the neat membrane. The lower efficiency for neat PVDF membrane, particularly with higher BSA concentrations, due to their hydrophobicity and poor antifouling characteristics. The optimal concentration of MXene (0.2%) demonstrates the importance of tuning membrane properties with nanoadditives. This can help further optimize the modification techniques for PVDF membranes to enhance protein removal efficiency, especially in applications requiring consistent performance across different concentrations.

**3.2.5. Assessment of tetracycline solution filtration.** To investigate the impact of blending MXene nanosheets with PVDF on the adsorptive removal performance, for organic micropollutants, the prepared membranes were used to separate tetracycline as a model of antibiotics. Fig. 7a and b shows the permeance and removal efficiency for 50, 100 mg $L^{-1}$ tetracycline solutions. The solution permeance and removal efficiency for tetracycline significantly enhanced after modification, particularly at lower concentration (50 mg $L^{-1}$). Fig. 7a, compares the permeance of tetracycline solutions through neat and modified PVDF membranes with MXene nanosheets. As tetracycline is introduced into the solution, the permeance typically decreases compared to that for pure water due to the interactions with the membrane material, likely by adsorption and aggragation. Higher concentrations of tetracycline lead to more adsorption and fouling, reducing permeance further. As shown in the figure, adding MXene nanosheets to the PVDF membrane modified the membrane structure, increasing the permeance due to the creation of more porous, hydrophilic pathways through the barrier layer and in the entire porous support part of the membrane. The inclusion of MXene nanosheets not only improves the permeation characteristics for water, but also enhances the adsorption effects for tetracycline, particularly at higher concentrations of MXene.[43] Consideration of these points provided insights into the improved functionality of the modified PVDF-MXene membrane system.

As shown in Fig. 7b, membrane M2 provided the best tetracycline removal, followed by M1 and M3, while the neat PVDF membrane (M0) exhibited the poorest efficiency, 25.4% and 18.33% at 50, 100 mg $L^{-1}$ tetracycline concentrations, respectively, due to their hydrophobic nature and lack of functional groups that can adsorb tetracycline effectively. Modifications to PVDF due to incorporation of new MXene functional groups that interact with tetracycline enhanced the removal efficiency up to 51%, 85%, 82% at 50 mg $L^{-1}$ tetracycline with 0.1%, 0.2%, 0.3% MXene content, respectively. The performance of these membranes differs based on how well these modifications enable interaction with tetracycline molecules. At a higher concentration, the removal efficiency decreased slightly, 42–64%, because saturation of the binding sites occurs to a larger extent (it should be noted that in each experiment the same volume, *i.e.*, 25 mL feed, has been filtered; see Section 2.4.2).

© 2025 The Author(s). Published by the Royal Society of Chemistry

Open Access Article. Published on 11 August 2025. Downloaded on 8/28/2025 4:21:29 AM.
This article is licensed under a Creative Commons Attribution-NonCommercial 3.0 Unported Licence.

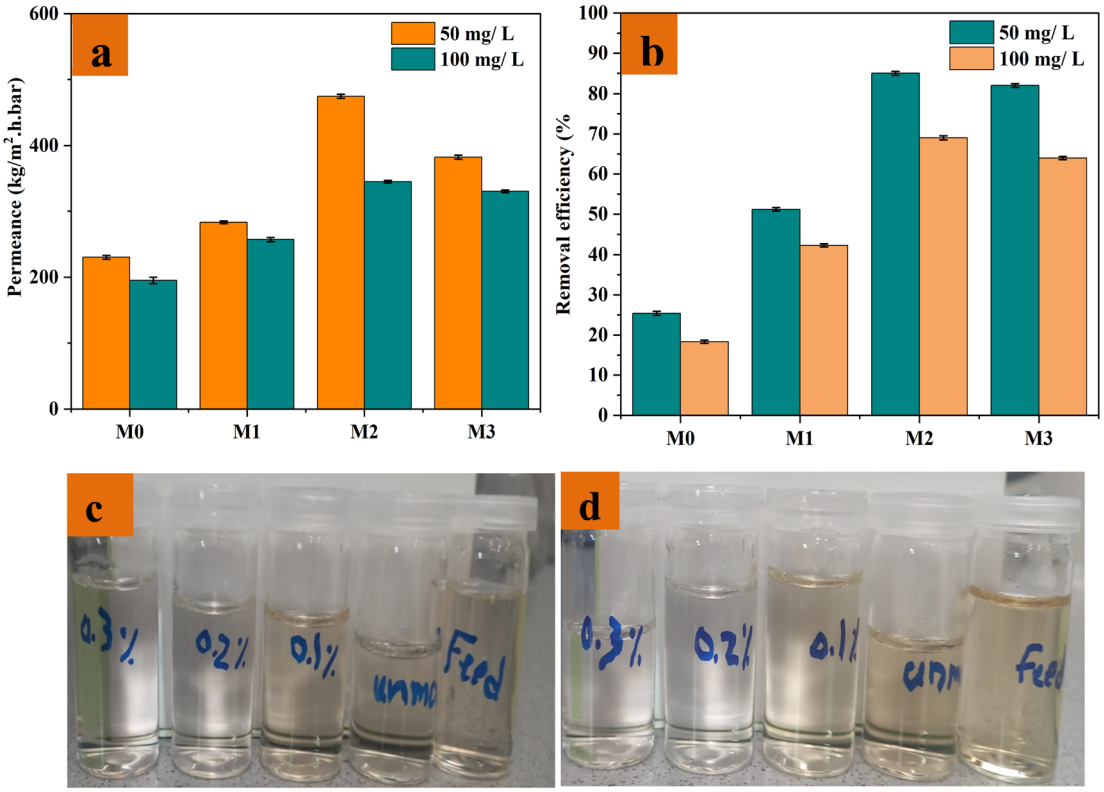


Fig. 7 (a) Permeance during tetracycline solution filtration, (b) tetracycline removal efficiency of the unmodified and modified membrane samples towards 50 mg $L^{-1}$, 100 mg $L^{-1}$, (c) and (d) digital photographs of permeate after the separation of 50 mg $L^{-1}$, 100 mg $L^{-1}$ tetracycline; respectively.

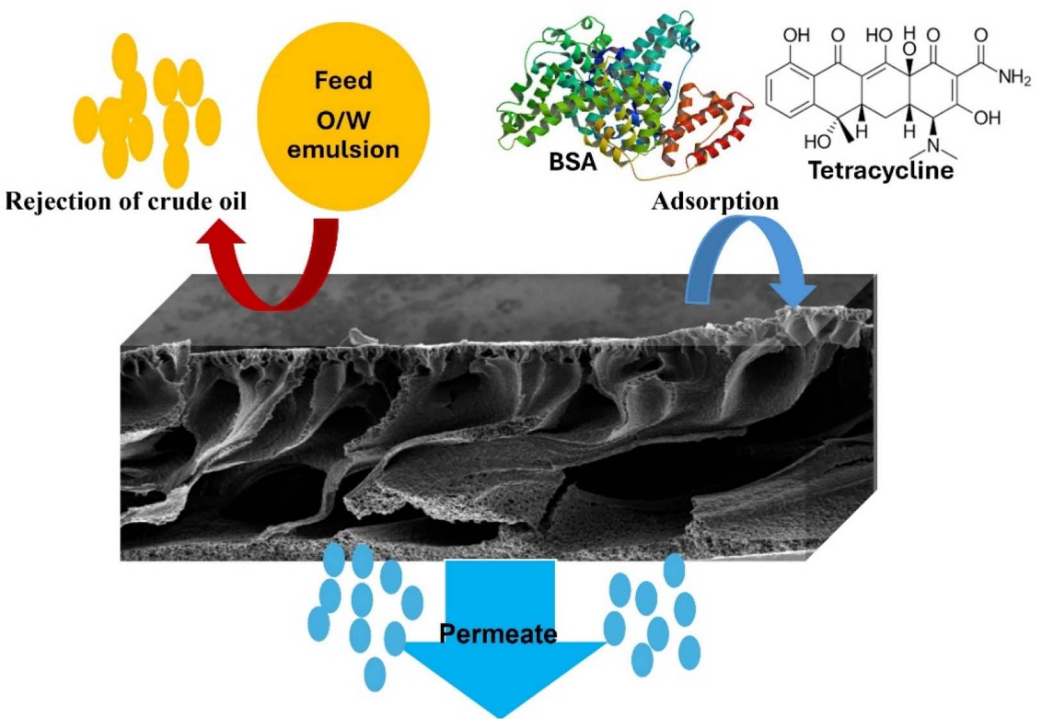


Fig. 8 Schematic description for separation mechanisms: size exclusion and adsorption.


© 2025 The Author(s). Published by the Royal Society of Chemistry

Open Access Article. Published on 11 August 2025. Downloaded on 8/28/2025 4:21:29 AM.
This article is licensed under a Creative Commons Attribution-NonCommercial 3.0 Unported Licence.

Membrane M2 maintained relatively high removal efficiency, 64%, because its structure and properties seem to be optimal also for tetracycline removal. This reflects the impact of nanofiller, especially in the case of M0 and M3, where either no additive or less accessible/aggregated filler led to faster saturation of adsorber capacity and more rapid decline in removal efficiency at higher tetracycline concentrations. Fig. 7c and d show visual comparison of the feed and permeate after separation of 50 mg $L^{-1}$ and 100 mg $L^{-1}$ tetracycline solutions through neat and modified PVDF membranes with MXene nanosheets. The digital photos provide a straightforward visual representation of the membrane's effectiveness in removing tetracycline from the solution.

**3.2.6. Separation mechanisms of PVDF mixed matrix membranes and performance comparison with state-of-the-art PVDF-based membranes.** The separation performance of the MXene@PVDF nanocomposite membranes is governed by a synergistic combination of size exclusion and adsorption-based interactions, as illustrated in Fig. 8. In oil–water emulsion, separation primarily depends on size exclusion, where the incorporation of MXene nanosheets into the PVDF matrix leads to the formation of narrower and more tortuous pores. This structural refinement, as indicated by porometry and SEM analysis, enhances the membrane's ability to block oil droplets while allowing water to permeate. Additionally, the improved hydrophilicity of the membrane surface due to MXene functional groups helps reduce oil adhesion and facilitates water transport through the membrane.

For protein separation, represented by BSA, the rejection mechanism is primarily governed by surface interactions rather than size exclusion. Although the nominal membrane pore size is close to the microfiltration range, the rejection of BSA likely arise from partial adsorption on the membrane surface. This interaction is attributed to the presence of functional groups and active sites on the MXene surface, which can facilitate interactions such as van der Waals forces and hydrogen bonding with protein molecules.

In the case of tetracycline, which is a smaller organic molecule, adsorption plays a dominant role. The MXene nanosheets offer a high density of surface-active sites capable of forming π–π interactions, and hydrogen bonds with tetracycline molecules. This leads to their efficient retention even though the molecule size is smaller than the nominal pore size. The relatively high surface area and chemical reactivity of MXene contribute significantly to this behavior. This multi-mechanism filtration strategy enables the prepared membranes to simultaneously achieve excellent rejection for a wide range of pollutants, including emulsified oil, proteins, and antibiotics.

To validate the superiority of the prepared $Ti_3C_2T_x$/PVDF membrane, a comprehensive comparison with previously reported PVDF-based membranes for wastewater treatment is presented in Table 2. The results clearly demonstrate that our membrane exhibits a notably higher water permeance (1242 L $m^{-2}$ h per bar), while maintaining excellent rejection (99%) and antifouling performance (FRR: 92%). The performance surpasses many previously reported PVDF-based membranes, without the need for complex synthesis steps or surface

Table 2 Summary of PVDF-based membranes for wastewater treatment

| Membrane | Fabrication method | Water permeance (L $m^{-2}$ h per bar) | Pollutant type | FRR (%) | Rejection (%) | References |
|---|---|---|---|---|---|---|
| ZIF-9-III@PVDF | Blending | 14.3 | O/W emulsion heptane | — | 99 | 67 |
| 1-Hexyl-3-methylimidazolium bis (trifluoromethylsulfonyl) imide ionic liquid (IL)@$Ti_3C_2T_x$/PVDF | Blending | 153 | BSA | 85 | 96 | 45 |
| Poly(ethylene glycol) methyl ether methacrylate-grafted $SiO_2$ ($SiO_2$-g-PEGMA) nanoparticles (NPs)/PVDF | Blending | 100 | O/W emulsion crude oil, BSA | 95 | 89 | 68 |
| Sodium alginates@$Ti_3C_2T_x$/commercial PVDF | Vacuum filtration | 887 | O/W emulsion kerosene, crude oil, hexane, heptane and petroleum ether | — | 99.4 | 44 |
| Na-montmorillonite ($Na^+$ MMT)/PVDF | Blending | 391.8 | O/W emulsion epoxy soybean oil | 98.1 | 98 | 69 |
| UiO-66-$NH_2$ with perfluoroalkyl polyethoxy acetic acid (FPEOAA)/PVDF | Grafting | 1403.5 | O/W emulsion petroleum ether, soybean oil, *n*-hexadecane and dichloromethane | 93 | 99 | 28 |
| Sodium polyacrylate (PAAS)/PVDF | Blending | 350 | O/W emulsion soybean oil, diesel oil and crude oil | 86.5 | 99.97 | 70 |
| $Ti_3C_2T_x$/PVDF | Blending | 1242 | O/W emulsion crude oil | 92 | 99 | This work |

Open Access Article. Published on 11 August 2025. Downloaded on 8/28/2025 4:21:29 AM. This article is licensed under a Creative Commons Attribution-NonCommercial 3.0 Unported Licence.

modification procedures. This confirms that the integration of MXene enhances membrane efficiency through both morphological and interfacial improvements, making it a promising candidate for practical applications.

## 4. Conclusions

The incorporation of MXene nanosheets into a PVDF membrane to construct mixed matrix membrane with significant improvements in wastewater treatment performance has been accomplished. The enhanced membrane provides superior filtration efficiency, combining size exclusion and adsorptive removal mechanisms to effectively separate a range of pollutants such as oil droplets, BSA (as model for macromolecular organic matter), and tetracycline (as example for a pharmaceutical micropollutant). MXene nanosheets introduce further hydrophilicity and increase water permeance, resulting in highest pure water permeance of 1242 kg $m^{-2}$ h per bar with 0.2% in the membrane casting solution. The nanosheets improve barrier pore structure and enhance surface properties, enabling efficient size exclusion for larger contaminants such as oil with maximum rejection of 99%. The hydrophilic nature of MXene enhances the membrane's resistance to fouling, reducing the adhesion of oil droplets and organic molecules on the membrane surface. This results in longer membrane lifetimes and more stable performance after three cycles of oil-in-water emulsion filtration. The large surface area, and functional groups on MXene nanosheets contribute to their adsorptive removal capacity. This makes the membrane highly effective in removing small organic pollutants like tetracycline, reducing their concentration in the permeate. The MXene@PVDF membrane is capable of treating various types of wastewater contaminants, from large emulsified oils to smaller organic pollutants due to its enhanced filtration efficiency, adsorption capabilities, and anti-fouling properties, making it suitable for diverse wastewater treatment applications such as industrial effluents, pharmaceuticals, and oil-water separation. The integration of MXene into traditional membrane technology paves the way for more efficient, long-lasting, and versatile treatment systems in water purification applications.

## Conflicts of interest

The authors declare no conflict of interests.

## Data availability

Upon reasonable request, raw data regarding this work can be requested through the corresponding author.

Supplementary information is available. See DOI: **https://doi.org/10.1039/d5ra03649f**.

## Acknowledgements

We would like to extend our sincere gratitude to the financial support provided by the Egyptian Ministry of Higher Education (MoHE) scholarship at Egypt-Japan University of Science and Technology (E-JUST) which supported the research by providing the facilities and labs required to conduct this study. We acknowledge the financial support of DAAD from the fund of BMZ through the We-AFRICA project No. 57708984. We are also grateful for the additional support provided by AfriGer-SDG DAAD project.

## References

1 B. J. Singh, A. Chakraborty and R. Sehgal, *J. Environ. Manage.*, 2023, **348**, 119230.
2 R. Song, W. Han, Z. Yang, Z. Ye, Y. Yang, H. Zheng, S. Zhao and G. Zeng, *J. Water Process Eng.*, 2025, **69**, 106614.
3 J. Willet, K. Wetser, J. Vreeburg and H. H. M. Rijnaarts, *Water Resour. Ind.*, 2019, **21**, 100110.
4 K. Ji, C. Liu, H. He, X. Mao, L. Wei, H. Wang, M. Zhang, Y. Shen, R. Sun and F. Zhou, *Polymers*, 2023, **15**, 741.
5 Z. Samavati, A. Samavati, P. S. Goh, A. Fauzi Ismail, N. Yusof, M. Sohaimi Abdullah, N. Hashim, N. D. A. P. Kerisnan, N. K. E. M. Yahaya and A. Idris, *J. Environ. Chem. Eng.*, 2024, **12**, 111696.
6 X. Huang, F. Pi, C. Zhou and X. Fu, *J. Water Process Eng.*, 2024, **57**, 104672.
7 T. Guo, J. Englehardt and T. Wu, *Water Sci. Technol.*, 2014, **69**, 223–234.
8 E. Obotey Ezugbe and S. Rathilal, *Membranes*, 2020, **10**, 89.
9 Y. J. Lim, S. M. Lee, R. Wang and J. Lee, *Membranes*, 2021, **11**, 508.
10 M. Awwad, M. Bilal, M. Sajid, M. S. Nawaz and I. Ihsanullah, *J. Environ. Chem. Eng.*, 2023, **11**, 109073.
11 N. H. Othman, N. H. Alias, N. S. Fuzil, F. Marpani, M. Z. Shahruddin, C. M. Chew, K. M. David Ng, W. J. Lau and A. F. Ismail, *Membranes*, 2021, **12**, 30.
12 N. A. Khan, S. Singh, E. A. López-Maldonado, P. Narasimhappa, P. F. Méndez-Herrera, J. R. López-López, U. Baig, P. C. Ramamurthy, N. M. Mubarak, R. R. Karri and I. H. Aljundi, *Desalination*, 2023, **565**, 116873.
13 S. Munirasu, M. A. Haija and F. Banat, *Process Saf. Environ. Prot.*, 2016, **100**, 183–202.
14 Z. Yang, P.-F. Sun, X. Li, B. Gan, L. Wang, X. Song, H.-D. Park and C. Y. Tang, *Environ. Sci. Technol.*, 2020, **54**, 15563–15583.
15 M. A. Alhussaini, B. M. Souza-Chaves, V. Felix and A. Achilli, *Desalination*, 2024, **586**, 117822.
16 H. Feng, J. Liu, Y. Mu, N. Lu, S. Zhang, M. Zhang, J. Luan and G. Wang, *Sep. Purif. Technol.*, 2021, **266**, 118586.
17 Z. Liao, Y. Wu, S. Cao, S. Zhao, X. Yan, S. Yuan, K. Dong, J. Qin, C. Ou and J. Zhu, *Sep. Purif. Technol.*, 2023, **308**, 122911.
18 F. Chen, Y. Sun, H. Wang, H. Yan, X. Chen, W. Lu and W. Chen, *React. Funct. Polym.*, 2023, **190**, 105639.
19 J. Chen, Q. Yu, M. Wang, D. Liu, L. Dong, Z. Cui, B. He, J. Li and F. Yan, *Sep. Purif. Technol.*, 2024, **330**, 125420.
20 D. Zou and Y. M. Lee, *Prog. Polym. Sci.*, 2022, **128**, 101535.
21 K. Fan, N. Kong, J. Ma, H. Lin, C. Gao, J. Lei, Z. Zeng, J. Hu, J. Qi and L. Shen, *J. Environ. Manage.*, 2024, **351**, 119922.
22 D. Suresh, P. S. Goh, A. F. Ismail and N. Hilal, *Membranes*, 2021, **11**, 832.


© 2025 The Author(s). Published by the Royal Society of Chemistry

Open Access Article. Published on 11 August 2025. Downloaded on 8/28/2025 4:21:29 AM. This article is licensed under a Creative Commons Attribution-NonCommercial 3.0 Unported Licence.

23 B. Ladewig and M. N. Z. Al-Shaeli, *Fundamentals of Membrane Bioreactors*, Springer Singapore, Singapore, 2017.
24 A. M. A. Abdelsamad, M. Matthias, A. S. G. Khalil and M. Ulbricht, *Sep. Purif. Technol.*, 2019, **228**, 115767.
25 W. A. Jonkers, E. R. Cornelissen and W. M. De Vos, *J. Membr. Sci.*, 2023, **669**, 121234.
26 X. Zhao, J. Li, S. Mu, W. He, D. Zhang, X. Wu, C. Wang and H. Zeng, *Environ. Pollut.*, 2021, **268**, 115705.
27 R. Ghanbari, P. K. Kahriz and H. Mahdavi, *Mater. Chem. Phys.*, 2022, **292**, 126751.
28 S. Shen, Y. Shen, Y. Wu, H. Li, C. Sun, G. Zhang and Y. Guo, *Chem. Eng. Sci.*, 2022, **260**, 117934.
29 M. Rostami, D. Jahani Sabet and V. Vatanpour, *Sep. Purif. Technol.*, 2022, **303**, 122226.
30 X. Bai, P. Liu, X. Gao, K. Liu, A. Li, Z. Lyu and Q. Li, *Mater. Chem. Phys.*, 2023, **301**, 127657.
31 S. Selambakkannu, N. L. Ishak, N. M. Fauzi, N. Ismail and Z. A. Karim, *Chin. J. Chem. Eng.*, 2024, **76**, 49.
32 M. Naguib, M. W. Barsoum and Y. Gogotsi, *Adv. Mater.*, 2021, **33**, 2103393.
33 M. Downes, C. E. Shuck, B. McBride, J. Busa and Y. Gogotsi, *Nat. Protoc.*, 2024, **19**, 1807–1834.
34 M. I. H. Protyai and A. Bin Rashid, *Heliyon*, 2024, **10**, e37030.
35 S. Ponnada, M. S. Kiai, S. Yadav, A. Palariya, C. S. R. Vusa, R. S. C. Bose, A. Nehra, S. Datta, R. Pawar, G. S. Martynkova, S. Gadkari, S. Naskar and R. K. Sharma, *Appl. Mater. Today*, 2024, **39**, 102310.
36 L. Ding, Y. Wei, Y. Wang, H. Chen, J. Caro and H. Wang, *Angew. Chem., Int. Ed.*, 2017, **56**, 1825–1829.
37 Y. Sun, J. Lu, S. Li, C. Dai, D. Zou and W. Jing, *Sep. Purif. Technol.*, 2024, **331**, 125640.
38 Y.-L. Liu, D. Li, P. Cao, X. Yin, Q. Zeng and H. Zhou, *Mater. Today Phys.*, 2024, **44**, 101444.
39 Z. Pouramini, S. M. Mousavi, A. Babapoor, S. A. Hashemi, N. Pynadathu Rumjit, S. Garg, S. Ahmed and W.-H. Chiang, *Water*, 2023, **15**, 1267.
40 S. Sahu and D. Dhar Purkayastha, *Sep. Purif. Technol.*, 2024, **330**, 125486.
41 S. Sinha Ray, H. Singh Bakshi, R. Dangayach, R. Singh, C. K. Deb, M. Ganesapillai, S.-S. Chen and M. K. Purkait, *Membranes*, 2020, **10**, 140.
42 N. Wang, R. Zhang, K. Liu, Y. Zhang, X. Shi, W. Sand and B. Hou, *Nano Mater. Sci.*, 2024, **6**, 672.
43 X. Dao, H. Hao, J. Bi, S. Sun and X. Huang, *Ind. Eng. Chem. Res.*, 2022, **61**, 6028–6036.
44 H. Zhang, Z. Wang, Y. Shen, P. Mu, Q. Wang and J. Li, *J. Colloid Interface Sci.*, 2020, **561**, 861–869.
45 S. Chen, T. Wang, X. Zhuo, Y. Wang and L. Wu, *J. Environ. Chem. Eng.*, 2022, **10**, 108027.
46 R. Imsong and D. Dhar Purkayastha, *Sep. Purif. Technol.*, 2023, **306**, 122636.
47 M. Benchakar, L. Loupias, C. Garnero, T. Bilyk, C. Morais, C. Canaff, N. Guignard, S. Morisset, H. Pazniak, S. Hurand, P. Chartier, J. Pacaud, V. Mauchamp, M. W. Barsoum, A. Habrioux and S. Célérier, *Appl. Surf. Sci.*, 2020, **530**, 147209.
48 M. U. Hassan, S. Lee, M. T. Mehran, F. Shahzad, S. M. Husnain and H. J. Ryu, *J. Nucl. Mater.*, 2021, **543**, 152566.
49 O. Kayanja, M. A. Hassan, A. Hassanin, H. Ohashi and A. S. G. Khalil, *Process Saf. Environ. Prot.*, 2023, **171**, 55–70.
50 F. Gholami, S. Zinadini and A. A. Zinatizadeh, *J. Environ. Chem. Eng.*, 2020, **8**, 104482.
51 V. M. Hong Ng, H. Huang, K. Zhou, P. S. Lee, W. Que, J. Z. Xu and L. B. Kong, *J. Mater. Chem. A*, 2017, **5**, 3039–3068.
52 H. Hu and T. Hua, *J. Mater. Chem. A*, 2017, **5**, 19639–19648.
53 I. Shaheen, B. Akkinepally, I. Hussain, S. Hussain, P. Rosaiah, A. Qureshi and J. H. Niazi, *J. Energy Storage*, 2024, **87**, 111513.
54 Z. U. Rehman, K. Khan, S. Yao, M. Nawaz, A. Miotello, M. A. Assiri, T. Bashir, T. L. Tamang and M. S. Javed, *Mater. Today Chem.*, 2024, **40**, 102200.
55 R. Liu and W. Li, *ACS Omega*, 2018, **3**, 2609–2617.
56 Q. X. Xia, J. Fu, J. M. Yun, R. S. Mane and K. H. Kim, *RSC Adv.*, 2017, **7**, 11000–11011.
57 J. Wang, Y. Wang, Y. Wang, X. Li, C. Wu, T. Zhang, B. Tian, L. Qian, Y. Guo, L. Wu, L. Zheng, Y. Li and X. Ding, *Fuel*, 2024, **374**, 132493.
58 S. Vigneshwaran, P. Sirajudheen, R. B. Vignesh, D.-G. Kim and S.-O. Ko, *J. Environ. Chem. Eng.*, 2024, **12**, 112266.
59 J. Liew, S. Bashir, K. Ramesh and S. Ramesh, *Mater. Sci. Eng., B*, 2025, **314**, 118076.
60 R. Han, Y. Xie and X. Ma, *Chin. J. Chem. Eng.*, 2019, **27**, 877–883.
61 Z. Hu, Z. Yin, F. Guo and W. Yang, *J. Membr. Sci.*, 2023, **686**, 122026.
62 M. P. Bilibana, *Adv. Sensor Energy Mater.*, 2023, **2**, 100080.
63 X. Wang, Q. Xiao, C. Wu, P. Li and S. Xia, *Chem. Eng. J.*, 2021, **416**, 129154.
64 Z.-K. Li, Y. Liu, L. Li, Y. Wei, J. Caro and H. Wang, *J. Membr. Sci.*, 2019, **592**, 117361.
65 G. P. Lim, C. F. Soon, A. A. Al-Gheethi, M. Morsin and K. S. Tee, *Ceram. Int.*, 2022, **48**, 16477–16491.
66 P. Zhou, T. Wang, C.-H. Du, G. Wang, L. Wu, X. Jiang and H.-C. Guo, *J. Environ. Chem. Eng.*, 2023, **11**, 110252.
67 H. Saini, P. Kallem, E. Otyepková, F. Geyer, A. Schneemann, V. Ranc, F. Banat, R. Zbořil, M. Otyepka, R. A. Fischer and K. Jayaramulu, *J. Mater. Chem. A*, 2021, **9**, 23651–23659.
68 B. Saini, M. K. Sinha and S. K. Dash, *J. Water Process Eng.*, 2019, **30**, 100603.
69 Z. Lv, P. Xue, T. Xie, J. Zhao, S. Tian, H. Liu, Y. Qi, S. Sun and X. Lv, *Sep. Purif. Technol.*, 2023, **305**, 122516.
70 S. Gao, P. Liu and J. Jin, *Front. Membr. Sci. Technol.*, 2024, **3**, 1355773.